Experimental and numerical study of AA5086-H111 aluminum plates subjected to impact

Hakim Abdulhamid, Amélie Kolopp, Christophe Bouvet, Samuel Rivallant

Experimental and numerical study of AA5086-H111 aluminum plates subjected to impact

Hakim Abdulhamid, Amélie Kolopp, Christophe Bouvet, Samuel Rivallant*

Université de Toulouse; INSA, UPS, Mines Albi, ISAE; ICA (Institut Clément Ader). ISAE, 10 avenue Edouard Belin, 31055 Toulouse, France

ARTICLE INFO

Keywords:
Impact
Experimental
Numerical simulation
Optimization

ABSTRACT

An experimental and numerical study of medium-velocity impact (within the range of 120 m/s) has been conducted on thin AA5086-H111 aluminum square plates. Targets with different thicknesses (between 2.5 and 4 mm), stratifications and aluminum alloys have been normally impacted by projectiles with 30 mm diameter and 127 g weight. Experimental results show that a compromise is to be found between the alloy strength and ductility, taking into account the impact velocity and energy. Ductile aluminum like AA5086-H111 grade subjected to medium-velocity impacts, showed the best perforation resistance. A finite element analysis was carried out using the ABAQUS finite element code. Slightly modified versions of the Johnson–Cook models of flow stress and fracture strain were applied. A good correlation between experimental and numerical results was found. The effect of strain rate appears to be predominant in the rupture initiation for the aluminum under consideration. Stratification seems to be advantageous compared to monolithic solutions. However, there are limitations to this tendency.

1. Introduction

Structural impact and associated protective systems are widely developed in numerous fields, such as the energy, transport and military industries. The current research focuses on the best choice of materials and design optimization for a given dynamic loading. Impact performance of targets is mostly evaluated through the ballistic limit velocity, the presence and shape of fracture, the residual velocity and thus the loss of kinetic energy of the projectile. After impact, the residual deformation or the maximum indentation is measured. The dynamic impact instrumentation has to be able to measure very short events with a sufficient accuracy. Numerous methods can be applied (gauges, interferometers, high speed cameras…) but they have limitations: measurement speed, accuracy, localized measurement zone, etc. That is why numerical studies are often carried out in parallel with experimental tests in order to complete the analysis.

This study aims to identify and optimize aeronautical armored structures subjected to foreign object impacts (birdstrike, ice or engine debris) through experimental and numerical studies. These impacts are characterized by medium initial velocities and high energies (120 m/s, 1 kJ) compared to ballistic impacts. The protective solution has been chosen to resist with minimum weight and residual deformation and without perforation. Targets are mostly AA5086-H111 aluminum thin plates (from 2 to 4 mm) with monolithic and layered structures. They are used to establish some tendencies for architectural optimization.

AA5083-H116 is close to the chemical composition of the AA5086-H111 aluminum alloy and has been widely studied in the literature. Clausen et al. [1] carried out an extensive study on this alloy to characterize flow and rupture characteristics as function of strain rate, temperature, stress triaxiality and rolling direction of the plate. The calibration of Johnson–Cook constitutive relation and rupture model is achieved. The results illustrate anisotropy in flow stress, strength and ductility due to a crystallographic texture of the grain in the rolling direction. A significant softening effect is obtained for temperatures comprised between 100 and 200 °C. This alloy is also characterized by negative strain rate sensitivity for intermediate strain rates whereas softening and ductility increase is observed in high strain rates. Børvik et al. [2] studied the behavior of 20-mm thick AA7075-T651 aluminum plates and investigated the effect of high strain rate through dynamic impact tests with ogival projectiles. A slightly modified version of the Johnson–Cook constitutive model is applied. A comparison with similar impact tests on 20-mm thick AA5083-H116 aluminum plates [3] shows that even though the yield stress of AA7075-T651 is more than twice the yield stress of AA5083-H116, the ballistic limit is 20%

* Corresponding author. Tel.: +33 561338158; fax: +33 561338352.
E-mail addresses: amelie.kolopp@isae.fr (A. Kolopp), christophe.bouvet@isae.fr (C. Bouvet), samuel.rivallant@isae.fr (S. Rivallant).

higher for AA5083-H116 with 244 m/s. This result emphasizes the fact that aluminum ductility can play a major role in resistance to impacts. To complete this assumption, results of impact on ductile materials such as steel or other aluminum alloys (Weldox 460 E and AA1100-H15 respectively) can be mentioned [4,5]. For both studies, projectiles of different shapes with a common diameter of 19 mm were used. For hemispherical projectiles, papers report large bending deformation with significant thinning in the vicinity of the impact point. The deformation under the projectile matches the projectile shape. A circular crack is sometimes observed at the back of the target, predicting the formation and detachment of a circular cap. Gupta et al. [5] associate the increase in the target deformation due to the hemispherical shape of the projectile with an increase of energy absorption.

There are many numerical simulations available in the literature. Based on the numerical and experimental study of Børvik [4,6], Teng et al. [7] evaluated the capability of different fracture models applied to ductile rupture under high velocity loading. They found that Johnson–Cook and Bao-Wierzbicki fracture models are able to predict the rupture pattern with a good approximation of the residual velocity. Most material models and rupture criteria are based on the Johnson–Cook expressions with occasional and slight modifications [2,5,8–11]. Grytten et al. [8] showed that low-velocity impacts can be reasonably well predicted without considering the effects of strain rate and temperature. However, the material behavior presents a stiffer response when omitting strain rate effects, and better results are obtained when including it. However, in the case of medium or high velocity impacts, the strain rate effect appears to have a major effect on rupture initiation. Some studies investigated the effect of stress triaxiality. Bao and Wierzbicki [12] associated large triaxialities with void growth as the dominant failure mode and negative stress triaxialities with shear failure. Based on tensile and upsetting tests, they defined a cut-off value of the stress triaxiality equal to $-1/3$, beyond which fractures do not occur. The influence of anisotropy of the material due to the rolling process appears to be insignificant. Iqbal et al. [10] carried out numerical simulations on monolithic 12-mm steel Weldox plates and on two 6-mm thick layers on the one hand and 1-mm 1100-H12 aluminum alloy and 0.5-mm double layered combinations on the other hand. Monolithic targets are found to have higher ballistic resistance than that of the layered in-contact targets with equivalent thickness.

Many studies investigated the possibility of improving impact performance by layering the targets, which offers a wide range of material and thickness configurations. However, the benefits of stratification are still not clear since the experimental parameters differ from one study to another: the projectile nose shape and velocity, the target materials and thicknesses [13,14]. Gupta et al. [13] showed that 1100-H12 aluminum monolithic structures have a better impact resistance than layered targets with the same total thickness (1–3 mm). These results are obtained with flat, ogival and hemispherical projectiles impacted at velocities between 33 and 126 m/s. Corran et al. [15] observed the same tendency for steel plates with a thickness lower than 3.5 mm. In this study, steel and aluminum targets are impacted using blunt and cylindro-conical projectiles with an impact velocity from 50 to 250 m/s. However, the results show that stratification appears to be advantageous above a total thickness of 6 mm. This tendency is confirmed by the studies of Teng et al. [16] and Dey et al. [17] on 12-mm thick Weldox 700E with flat projectiles. They showed that the perforation resistance can be improved by about 7–25% with the use of two layers of 6 mm without any adhesion. Also note that in the case of layers of different thicknesses, the combination of a thin layer preceding the thicker one offers more resistance against perforation [15]. More generally, the impact tests conducted by Teng et al. [18] on the association of ductile Weldox 460E and another ultra-high strength steel, concluded that the configuration with the ductile material as the first layer gives the best performance.

In this paper, firstly experimental impact tests and results are presented (Sections 2 and 3). Secondly, finite element models based on the experimental tests are described (Section 4). Comparisons between the experimental and numerical data and discussions are given in Section 5, and finally, a preliminary numerical study of structure optimization is given in Section 6.

2. Impact tests

2.1. Experimental set-up

Impact tests have been conducted with a gas gun on aluminum targets at an average velocity of 120 m/s. The target is simply supported at the rear by a square frame with an aperture of 170-mm side (see Fig. 1a). These boundary conditions are more representative of impact on real structures like the aircraft fuselage compared to clamping along four edges. The projectile used is composed of a cylindrical hardened steel nose with 30 mm diameter. A cylindrical shank with 8 mm diameter and 50 mm length is screwed to the rear of the nose (see details in Fig. 2). The same projectile is reused for all impact tests. During the impact test, the projectile displacement is measured with a high speed camera at 75 frames/ms. A post-processing program is used to detect the projectile during the impact thanks to the painted shank and calculate the instantaneous velocity (Fig. 1b).

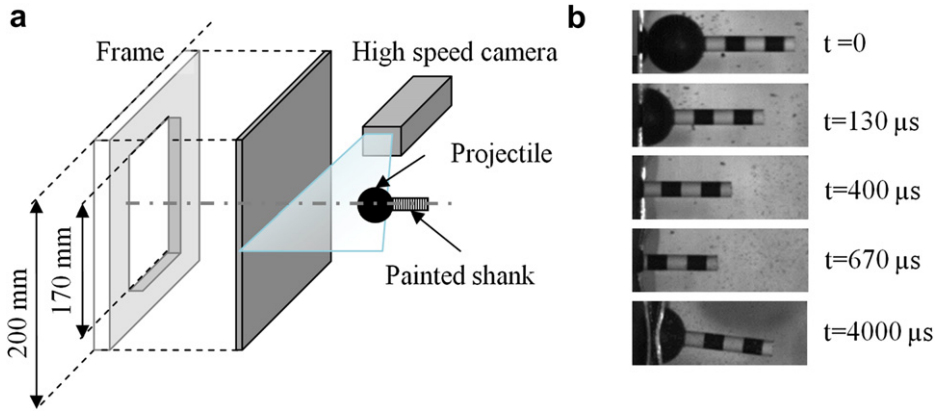

Fig. 1. (a) Experimental set-up; (b) camera pictures of the projectile during impact.

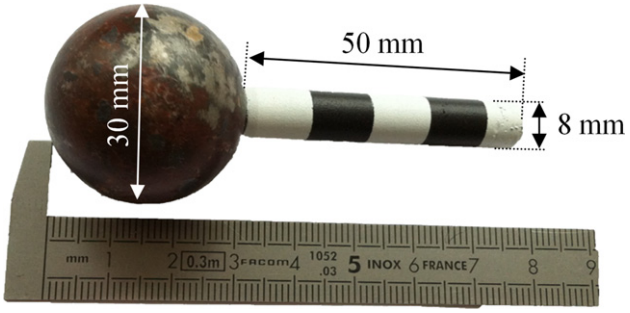

Fig. 2. Projectile used in experimental impact tests.

2.2. Test panels

Normal impact tests have been conducted on different configurations of AA5086-H111 aluminum plates (Table 1). Square targets of different dimensions (200, 300 and 400 mm sides indicated by A, B and C respectively) are impacted at the center of the plates. Monolithic structures are compared to layered targets with the same total thickness, to identify the best configurations through the observation of rupture and the distribution of residual deformations. The total thickness h_t is comprised between 2 and 4 mm, from monolithic structures to five-layered structures. The number of layers and the corresponding thicknesses are indicated in the index of names beginning by the front skin. When several similar configurations are tested, an exponent is added to each target number. The layers can either be simply superposed or assembled together with an adhesive film (Redux 609-300, 300 g/m^2, aeronautical certified resin) to evaluate the bonding influence.

3. Experimental results and analysis

Impact test results are given in Table 2. The initial velocity shows dispersions due to the experimental set-up, so the initial kinetic energy E_{ini} can be substantially different from one sample to another. However, the initial projectile velocity V_{ini} is measured before the impact from the camera pictures for each configuration, so the variability is known and taken into account in the analysis. The positive values of residual velocity V_{res} indicate the velocity after perforation of targets while the negative values are measured during the projectile rebound. The maximum projectile displacement d_{max} is measured from the camera pictures. After impact, the residual profile is measured by 3D correlation for non-perforated samples and the residual indentation of the back layer I_{res} is also indicated (see in Table 2). The impact duration T_i is measured from the camera pictures. It represents the duration from the beginning of the projectile–target contact until the end of the contact in case of projectile rebound or target perforation (indicated by R_{front} and R_{back} to describe the rupture location). During the impact, the kinetic energy of the projectile is transformed into work through a diffuse stress wave transfer. Thus, one part of the initial energy is assumed to be absorbed by global target deformation, local plastic flow and failure, elastic work. The remaining energy represents the residual kinetic energy of the projectile. The absorbed energy corresponds to the kinetic energy loss of the projectile, i.e. the sum of internal energy absorbed by the plate through elastic and plastic mechanisms.

Table 1
Description of tested samples.

Samples	Dimensions [mm^2]	Layer thicknesses [mm]					Adhesive film	h_t [mm]	Weight per unit area [kg/m^2]
		Front	→			Back			
A_{1+1}	200 × 200	1				1	Yes	2	5.5
A_{2+1}	200 × 200	2				1	Yes	3	8.2
A_{2+2}	200 × 200	2				2	Yes	4	10.9
A_4	200 × 200			4			No	4	10.7
$B_{3\times1}$	300 × 300	1		1		1	No	3	7.8
B_{2+1}	300 × 300	2				1	No	3	7.7
B_{1+2}	300 × 300	1				2	No	3	7.7
$B_{5\times0.5}$	300 × 300	0.5	0.5	0.5	0.5	0.5	No	2.5	6.7
C_{1+1}	400 × 400	1				1	Yes	2	5.5
C^1_{2+1}	400 × 400	2				1	Yes	3	8.3
C^2_{2+1}	400 × 400	2				1	Yes	3	8.2
C_3	400 × 400			3			No	3	8.0

Targets less than 3-mm thick are systematically perforated as shown in Fig. 3a and b. They failed through plug initiation and the formation of petals, which is a typical failure mode of ductile targets [5]. Two similar configurations of the critical thickness (3 mm) have been tested, namely C^1_{2+1} and C^2_{2+1}. The C^1_{2+1} sample, impacted at 122.6 m/s, shows a circular rupture at the rear of the target, extended only to the 1-mm thick plate (Fig. 3c). This particular result is not observed for a second identical target even though a higher initial velocity. The C^1_{2+1} configuration shown in Fig. 3c will be taken as a reference case for the calibration of the rupture model in numerical simulations, taken into consideration a possible material defect. Finally, a necking zone can be clearly seen near the impact point at the back of non-perforated samples (Fig. 3d).

Perforated samples show high local plastic deformations, thinning of the plates under the projectile, and petals formation. However, the out-of-plane residual deformations in the rest of the plate are lower than those in the non-perforated cases. It may be due to the fact that global plate reaction and plasticity did not have time to spread enough before rupture initiation. This results in a lower amount of absorbed energy. It can be seen from experimental results that plate perforation, impact duration and residual velocity are directly linked. Generally speaking, the impact duration is inferior to 0.49 ms for perforated targets and superior to 0.72 ms for non-perforated targets. Note also a global tendency for impact duration to increase with decreasing plate dimensions (see details in Section 5.1). The limit is reached for 200-mm square targets which show residual deformations up to the plate boundary. This leads to greater plate deformations and absorbed energy through the plate boundary rotation, which cannot be representative of real aeronautical structures (see Fig. 4a). A lower plate dimension limit has therefore been set to square targets of 300-mm side to avoid undesirable effects of boundary conditions for the future tests (as shown in Fig. 4b).

4. Finite element simulations

4.1. Finite element model

The numerical simulation of the impact problem is carried out using the commercial software ABAQUS 6.9-2/Explicit. The material constitutive law is implemented in a user-defined subroutine VUMAT. The projectile used in experimental tests is composed of a hardened steel nose and shank. No bending deformation of the shank is observed during the impact due to the shank geometry and its negligible mass compared to the nose mass. Considering these points and the fact that the targets are sufficiently thin compared to the projectile geometry, the latter is supposed to be rigid [23]. In the numerical model, the projectile is therefore represented by an analytical rigid body of the same diameter with the corresponding mass of the sphere and the shank. The finite element model represents a 1/8th portion of the target. Symmetric boundary

Experimental and numerical results.

Samples	A_{1+1}	A_{2+1}	A_{2+2}	A_4	$B_{3\times1}$	B_{2+1}	B_{1+2}	$B_{5\times0.5}$	C_{1+1}	C^1_{2+1}	C^2_{2+1}	C_3
Experimental results												
E_{ini} [J]	948	987	1018	923	856	973	999	1007	946	954	983	884
V_{ini} [m/s]	122.2	124.6	126.6	120.6	116.1	123.8	125.4	126.0	122.0	122.6	124.4	118.0
V_{res} [m/s]	60.6	−12.7	−9.3	−14.5	−9.8	−11.7	−14.0	83.0	66.3	−21.5	−22.4	−21.4
R_{front}	Yes							Yes	Yes			
R_{back}	Yes							Yes	Yes	Yes		
d_{max} [mm]	/	53.4	41.1	37.1	40.6	39.4	39.8	/	/	37	37.2	35.6
I_{res} [mm]	/	48.9	31.6	33.8	37.5	32	35.5	/	/	30.6	31.5	30
T_i [ms]	0.4	1.21	0.92	0.89	0.95	1.07	1.0	0.32	0.49	0.76	0.76	0.72
Numerical results												
V_{res} [m/s]		−12.2	−12.7		−15.6	−19.3	−16.9	80.7	71	−24.4		−24.5
R_{front}								Yes	Yes			
R_{back}								Yes	Yes	Yes		
d_{max} [mm]		40.7	32.9		34	35.4	35.8	/	/	33.2		31.7
I_{res} [mm]		36.1	31.4		31.1	31.6	33.13	/	/	30.3		28.5

conditions are imposed on the edges of the sample and the rear side is simply supported by the frame, as shown in Fig. 5. We assume that the adhesive film between the skins behaves as a perfect bond. The contact between the projectile and the plate is modeled using the penalty contact algorithm. The contact friction between the projectile and the front plate on the one hand and the rear plate and the frame support on the other hand are neglected. The model is meshed using a linear brick element with reduced integration (C3D8R), and default hourglass is used to prevent excessive distortion of elements. The model is subdivided into four sub-regions Z1-Z4 with a decreasing mesh refinement (see Fig. 5). The boundaries between these zones correspond to respective radii of 10, 30, and 50 mm. The sides of the elements are approximately 0.2 mm, 0.5 mm, 2 mm and 2.5 mm from the Z1 to the Z4 zones.

4.2. Constitutive relation and fracture criterion

The initial full Johnson–Cook flow stress and fracture strain law depend on the triaxiality ratio, the strain rate, the temperature and the equivalent plastic strain, as given in equations Eqs. (1) and (2) [19]:

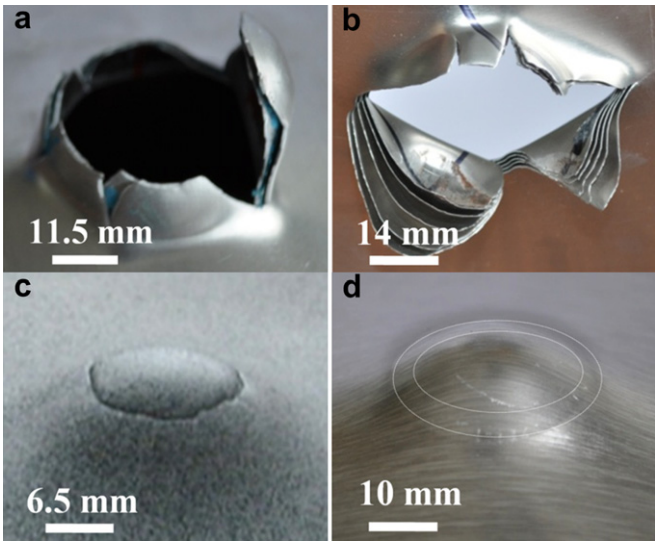

Fig. 3. Rupture shape of samples: (a) A_{1+1}; (b) $B_{5\times0.5}$; (c) C^1_{2+1}: Circular rupture of the back plate (14 mm diameter); (d) necking zone at the rear of $B_{3\times1}$ sample.

$$R(p) = (A + Bp^n)\left(1 + C\ln \dot{p}^*\right)\left(1 - T^{*m}\right) \quad (1)$$

$$\varepsilon^f = \left(D_1 + D_2\exp^{-D_3\sigma^*}\right)\left(1 + D_4\ln \dot{p}^*\right)(1 - D_5T) \quad (2)$$

The stress triaxiality σ^* is defined as the ratio of the mean hydrostatic stress and the von Mises equivalent stress. The temperature increase is represented by the ratio $T^* = (T - T_0)/(T_m - T_0)$ where T_0 and T_m are the room and melting temperatures respectively. The strain rate contribution is defined as $\dot{p}^* = \dot{p}/\dot{p}_0$, where $\dot{p}_0$ is a reference strain rate set to 1 s^{-1} and p represents the equivalent plastic deformation. The constants A–C, n, m, D_1–D_5 depend on the material properties. The yield stress values A and B, n (determined with the least squares' method) as well as D_1, D_2 and D_3 are measured from quasi-static tensile tests conducted on smooth and notched specimens of different radii [1]. The parameters are dependent upon the strain rate influence C and D_4 can be determined from quasi-static and dynamic tensile tests (using Split–Hopkinson tension bars for strain rates up to 100 s^{-1}). However, it will be seen later that several contributions can be neglected in this study.

A modification of these formulations is commonly done [1,19,20] and consists in replacing the strain rate contribution by the value $(1 + \dot{p}^*)^C$ in order to evaluate the flow stress and fracture strain in quasi-static loads. The influence of temperature increase on the flow stress and the rupture initiation has already been investigated in the literature. Conduction heat transfer is a slow process compared to the impact duration and the temperature rise in plastic zones is mainly adiabatic. In [24], Camacho et al. showed that the heat transfer is negligible in perforation cases even in case of thick targets (50-mm thick). However, the formation of a thin molten zone which acts as a lubricant in the contact target/projectile is mentioned. This result has been confirmed in this study with a fully coupled thermo-mechanical analysis using ABAQUS. An impact on a 2-mm thick aluminum plate at 125 m/s is modeled assuming an adiabatic heat transformation inside the elements, due to the very short impact duration. The highest temperature increase of the specimen is around 82 °C with an inelastic heat fraction of 0.9 (see Table 3), and corresponds to a localized area of the rear face of the plate. The effect of temperature increase on flow stress and rupture behavior is studied in [1], with 5083-H116 aluminum samples. It is shown that the behaviors at 20 °C and 100 °C are very similar while the effect of temperature increase appears to be significant above 200 °C. Based on the numerical results and the literature [24], we thus assume that the effect of the increase of temperature is negligible on the flow stress and rupture expression.

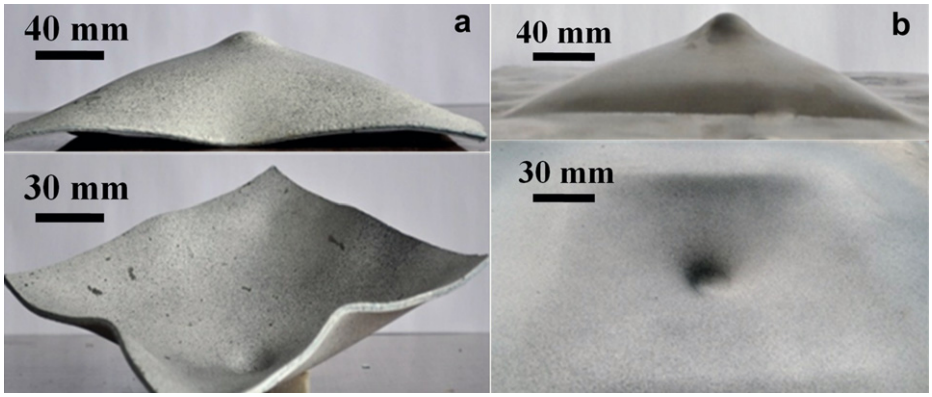

Fig. 4. Boundary deformations of: (a) A_{2+1}; (b) C^1_{2+1} samples.

4.3. Calibration of the Johnson–Cook constitutive model

Concerning the strain rate effect, it is mentioned in [1,21,22] that 5xxx aluminum alloys show negative strain rate sensitivity at low strain rates. This phenomenon is due to dissolved magnesium atoms diffusion which prevents dislocation movements and causes negative strain ageing. This effect based on atom diffusion is negligible under high strain rate loadings. Experimental points from [1] are given in Fig. 6 for AA5083-H116 alloy to illustrate this negative strain rate sensitivity. It can be seen in Fig. 6 that the flow stress decrease remains below 15% in the rolling direction and tends to take the initial values of quasi-static tests when reaching high strain rates (from 1000 s^{-1}, difference of 5% in flow stress). However, this particular behavior is not compatible with the strain rate expression $(1+\dot{p}^*)^C$. To avoid numerical instabilities due to a negative C value, this parameter is chosen slightly positive in [1]. The strain rate contribution is thus approximated by a constant mean value based on the high strain rate solicitation cases (represented by lines in Fig. 6). In numerical simulations (see further details in Section 5.1), the critical zone under the projectile is characterized by high strain rates (above 1000 s^{-1}). Therefore, the local mechanisms (plasticity, onset of rupture and cap formation) are not influenced by dynamic strain ageing, so this contribution is not considered in the model. The hypotheses evoked previously lead to a reduced form of the initial Johnson–Cook model as a simple power law hardening model: $R(p) = A + Bp^n$. The AA5086-H111 flow stress curves are thus obtained from quasi-static tensile tests under constant displacement rate. The specimen geometry is given in Fig. 7. Several tests are conducted along the three directions 0°, 45° and 90°, with respect to the rolling direction of the plate for each plate thickness: 2, 1 and 0.5 mm.

The strain is measured with a longitudinal extensometer and the true strain and true stress curves are obtained for each direction in Fig. 8. Since the 1-mm thick samples are very similar to the 2-mm thick ones in terms of plastic flow and rupture deformation, they are not represented in the figure. Note that for each sample thickness, the flow stress evolution is quite similar for each direction, except for the plastic strain at rupture. The rolling direction appears to be the most critical one, followed closely by the perpendicular direction. The 45° orientation shows a more ductile behavior. These observations are also mentioned in the study of Clausen et al. [1] for AA5083 aluminum and are associated with the texture modification during the rolling process. The difference in flow stress between the two thicknesses is due to the slight difference in the alloy composition of the 0.5-mm thick plates. As the flow stress evolution is very similar for each direction, we consider the material isotropic with the behavior of the rolling direction. The numerical flow stress curve is then obtained from the experimental measurements using the least square method. The values of A, B and n are indicated in Table 3.

4.4. Calibration of the rupture model

For convenience and better understanding of the parameters, the fracture strain expression in Eq. (2) is rewritten in Eq. (3) to highlight the independent contributions of static rupture deformation, triaxiality ratio and strain rate effect. Thus, the simplified expression is the following:

$$\varepsilon^f = \varepsilon^f_{1/3} \exp^{T(\sigma^* - (1/3))} (1+\dot{p})^V \tag{3}$$

The fracture strain $\varepsilon^f_{1/3}$ is obtained from quasi-static tensile tests conducted on AA5086-H111 aluminum samples. The parameters T and V are associated respectively with the triaxiality and the strain rate. The corresponding values used in the model are given in Table 3. Material failure is reproduced by element deletion in the

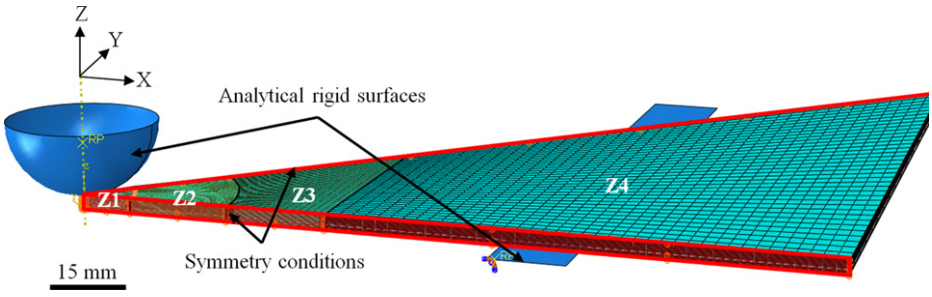

Fig. 5. Modeling parameters applied on a 1/8th portion of a 300-mm side length.

Table 3
Material parameters after calibration.

Elastic modulus, E (GPa)	70
Poison's ratio, υ	0.3
Density, ρ (kg/m^3)	2700
A (MPa)	143
B (MPa)	562
n	0.6
Heat capacity, C_p (J/kg K)	900
Inelastic heat fraction, α	0.9
$\varepsilon^{f}_{1/3}$	0.299
T	−0.483
V	0.086

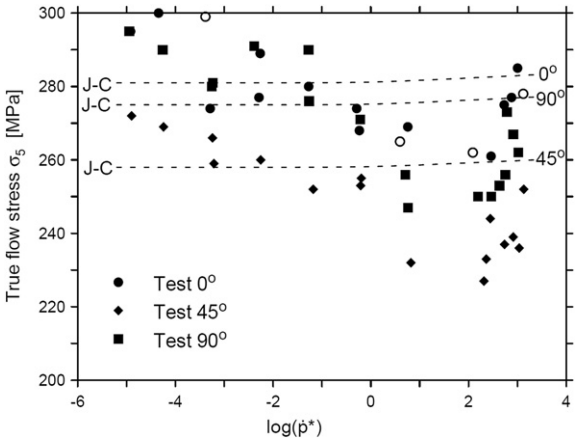

Fig. 6. Evolution of the true flow stress based on the strain rate, curve from [1].

model and is controlled by the failure criterion F defined in Eq. (4). The quantity $d\overline{\varepsilon^{P}}$ corresponds to the increment of the equivalent plastic strain and ε^{f} is the plastic strain at failure. The number of deleted elements is considered sufficiently low to neglect mass and energy losses due to numerical element erosion.

$$F = \int_0^t \frac{d\overline{\varepsilon^{P}}}{\varepsilon^{f}} dt = 1 \tag{4}$$

Experimental data measurements from [1] based on the stress triaxiality ratio are given in Fig. 9. These results are determined from quasi-static tensile tests conducted on AA5083-H116 aluminum plates in the rolling direction (smooth and notched samples of different radii have been tested to evaluate the stress triaxiality influence on rupture strain). The theoretical curve is determined by fitting the rupture strain measurements. An additional experimental data point is obtained from tensile tests conducted on AA5086-H111 aluminum. A slight variation of triaxiality effect is assumed between the AA5086-H111 and AA5083-H116 alloys, and the value of T chosen for this study is identified from [1] in the rolling direction (most critical case). The theoretical curve for AA5086-H111 is thus obtained from Eq. (3) with the values of $\varepsilon^{f}_{1/3}$, T

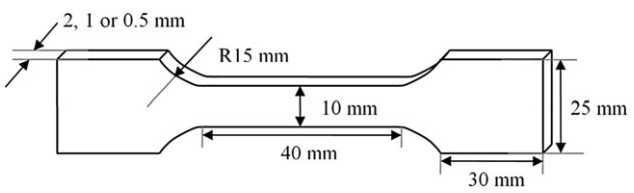

Fig. 7. Tensile test specimen geometry.

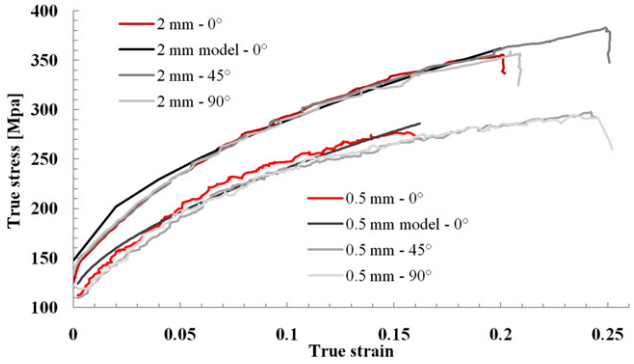

Fig. 8. Experimental quasi-static flow stress of AA5086-H111 and theoretical curve.

and V given in Table 3. A cut-off value is defined for triaxiality ratios lower than 1/3 [12], beyond which no rupture occurs. In this configuration, an arbitrary high fracture strain value is defined and is evaluated to 1 (see Fig. 9). The fracture strain of 100% is sufficient to avoid rupture due to compressive strains. It will be seen further that element deletion appears only in a zone situated at the rear of the back layer and characterized by bi-axial tensile stresses (triaxiality ratio around 0.6). However, no element is deleted in zones subjected to compressive loading.

The parameter $\varepsilon^{f}_{1/3}$ is determined from the rupture strain in the rolling direction during quasi-static tensile tests. This value is measured from the post-mortem section reduction in the fracture zone. Plastic deformation is assumed to occur at constant volume; therefore, any reduction in the local section induces a longitudinal strain to compensate the change in volume. This method gives the local strain evaluated to 0.299 as compared to the mean values obtained from the extensometer (Fig. 8), which are lower (0.201). Concerning the strain rate contribution, the parameter V is strongly dependent on the material heat treatment and microstructure. Thus, the parameter value is directly evaluated from experimental impact tests conducted on AA5086-H111 plates. The value is set to reproduce the particular ring crack observed in the C^{1}_{2+1} sample, as shown in Figs. 3c and 15b.

The evolution of fracture strain obtained versus the strain rate is given in Fig. 10. Experimental measurements from AA5083 quasi-

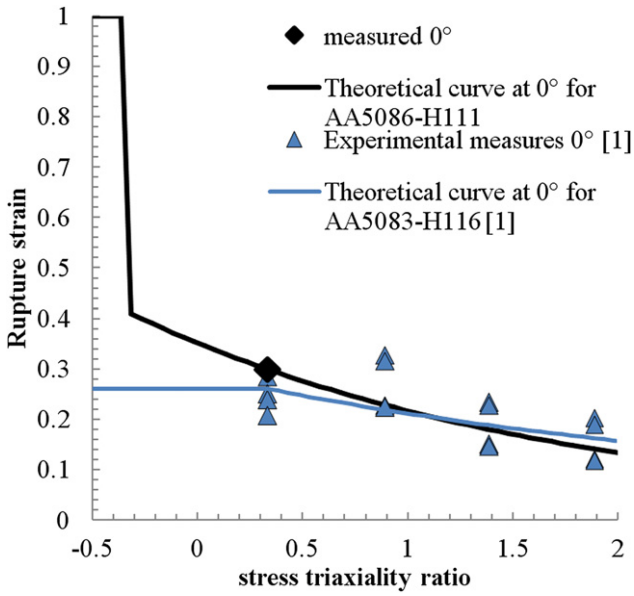

Fig. 9. Evolution of the equivalent fracture strain with the triaxiality ratio ($\dot{p} = 1$).

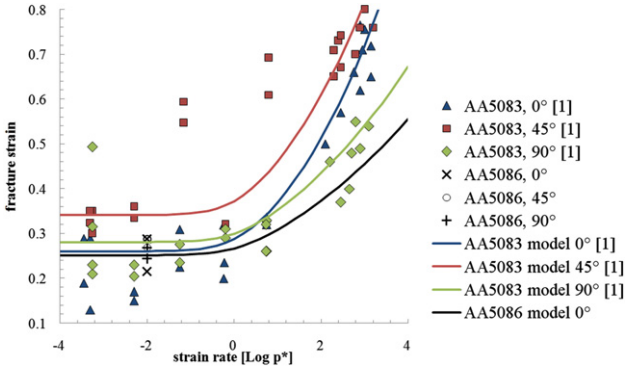

Fig. 10. Evolution of fracture strain versus the strain rate under uniaxial traction.

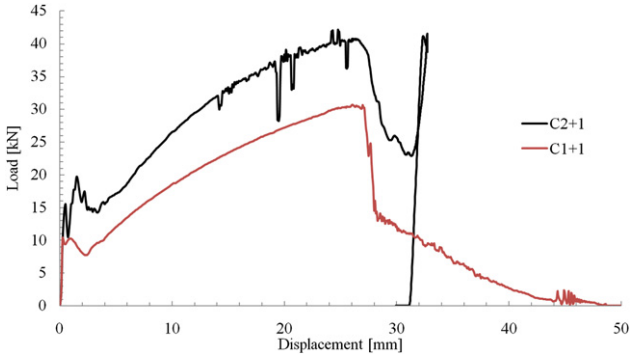

Fig. 12. Force versus displacement curve during the impact of C^1_{2+1} and C_{1+1} targets.

static tensile tests are plotted in the three directions. Theoretical curves are determined for each direction by fitting the curve to experimental results. Additional measurement points are given for AA5086-H111 alloy and the theoretical curve obtained in the rolling direction is added with the value of V given in Table 3. Though the curves in the most critical direction are very close for the two alloys, the fracture model is very sensitive to the strain rate, especially in the high strain rate domain (between 10^3 and 10^4 s^{-1}). To complete this calibration process, an analysis has therefore been undertaken to identify the sensitivity of the rupture initiation with respect to impact energy. On the one hand, it has been found that the rupture ring disappeared partially with an initial kinetic energy decrease of 50 J and totally with a decrease of 100 J. On the other hand, an energy increase of 150 J is necessary to perforate the structure. The material parameters of the flow stress and rupture models are summarized in Table 3.

5. Numerical results and comparison with experimental data

To validate the numerical model, simulations involving the set-up and target properties of A and C family samples (corresponding to targets of 200 mm and 400 mm sides respectively) have been implemented and analyzed. The projectile velocity evolution and penetration, the residual profile of the specimen and the rupture shape in case of perforation, are compared.

5.1. Impact sequence description

Several impact stages can be identified by numerical simulations in the case of projectile rebound, as shown in Fig. 11. The initial state is defined by the onset of contact between the projectile and the target. The first stage is one of the most important but also critical impact moment. High and local out-of-plane target deformations are observed under the projectile at the rear of each layer. The rupture criterion F increases rapidly in this zone, but this tendency is moderated by very high strain rates (between 500 and 4000 s^{-1}) which tend to delay the onset of the rupture. In the same time, the projectile velocity decreases strongly as shown in Fig. 13 and a large amount of energy is transferred to the target (decrease down to 250 µs for the C_{1+1} target and 450 µs in the A_{2+1} case). While the rupture is not initiated, the deformations propagate in the plane of the sample (see Step 1 in Fig. 11). It corresponds to the load increase zone at the beginning of the curve (see on Fig. 12 the projectile displacement between 4 and 26 mm). The first stage ends when the plastic deformations reach the support. Note that only one inflexion of the plate can be observed before this step. The second step corresponds to a global reaction of the plate, characterized by a stabilization of the rupture criterion and a decrease of the projectile contact pressure (due to the increase of the working area). A second inflexion appears in the plate near the support. A gradual decrease of projectile velocity is observed due to a global move of the target with structure bending. Note that the projectile braking is more or less consequent depending on the ability of the target to rotate in the vicinity of the boundary condition. For a same configuration (see for instance the difference

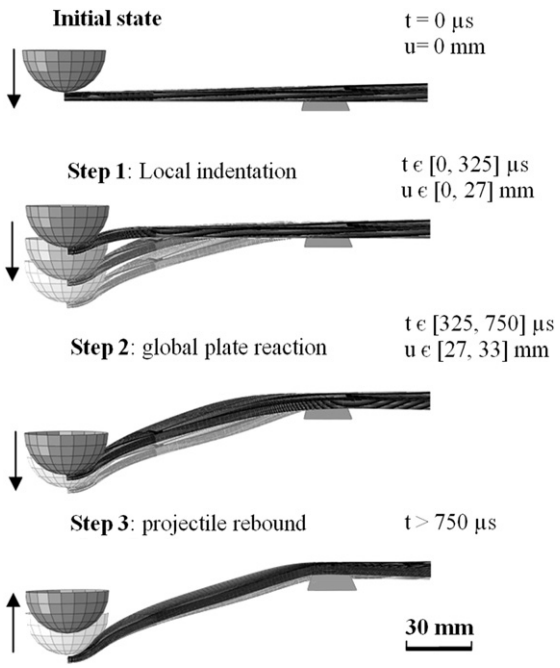

Fig. 11. Impact stages identification through the C^1_{2+1} example.

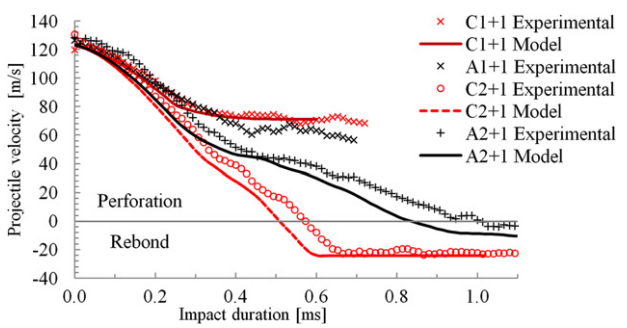

Fig. 13. Evolution of the projectile velocity during the impact.

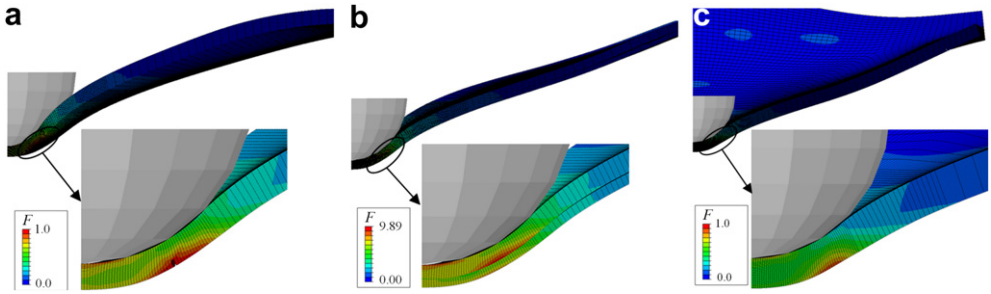

Fig. 14. Mapping of the rupture criterion F for different targets: (a) C^1_{2+1}; (b) B_{2+1}; (c) A_{2+2}.

between the A_{2+1} and C^1_{2+1} targets in the second part of the curve in Fig. 13), the rotation of 300 or 400 mm edge samples is prevented by inertial effects which offer a stronger resistance to the projectile displacement, and thus a faster braking. The last step consists in the projectile rebound and elastic springback of the plate. This can be seen in Fig. 12, through the final peak load preceding the separation of the projectile and the plate.

Note that the numerical results reasonably fit with the experimental measurement of projectile velocity (±5 m/s gap for the residual velocity prediction), in spite of a slight overestimation of the projectile braking. However, the model is quite accurate for perforation cases, which means a good prediction of the rupture initiation instant and failure propagation. In totally perforated cases (A_{1+1} and C_{1+1} samples), the residual velocities are around 70 m/s and the A_{1+1} sample absorbs slightly more energy than the same configuration with higher dimensions (see Fig. 13). This is due to inertia effects observed on samples with 300 mm and 400 mm edges, resulting in a stiffer global response of C_{1+1} compared to the A_{1+1} target.

5.2. Rupture criterion evolution and mapping during impact

The mapping and values of the failure criterion F are analyzed to localize the most critical area and to evaluate the state of vulnerability of each configuration. The most critical zone is a ring with a radius of approximately 6 mm. It is situated at the rear of the back plate under the projectile for bonded layers. If the layers are simply superposed, it is located at the rear of the thickest layer or at the rear of the first plate with similar layers (see Fig. 14a, b). Concerning undamaged targets, the higher criterion values are 0.83, 0.92 and 0.95 respectively for the C_{2+2}, A_{2+2} and A_{2+1}, localized at a distance of 7.2, 8.6 and 7.7 mm from the impact point (see for instance Fig. 14c).

The criterion limit F is reached only in the back plate thickness, in the reference configuration C^1_{2+1} used for calibration. In the numerical results, the first deletions of elements are initiated from 230 μs, just before the global structure effect. The final rupture shape is a ring of 14 mm diameter (see Fig. 15b), initiated at the rear face of the back plate and propagated out-of-plane up to the adhesive film (see Fig. 14a). This observation is consistent with the reality (see Fig. 15b). It corresponds to a zone where the bi-axial traction is the main stress (constant triaxiality ratio evaluated to 2/3, which is critical because of low rupture deformations as shown in Fig. 9). The failure propagates slowly due to the global structure effect up to 500 μs, which corresponds to the projectile rebound. The formation of secondary cracks perpendicular to the initial rupture shape can lead to the formation of petals in the case of a target perforation, as shown in Fig. 15a, c and d. Due to the symmetric conditions applied in the numerical model, the cap is completely removed from 260 μs in the numerical simulation while it remains partially attached in the reality.

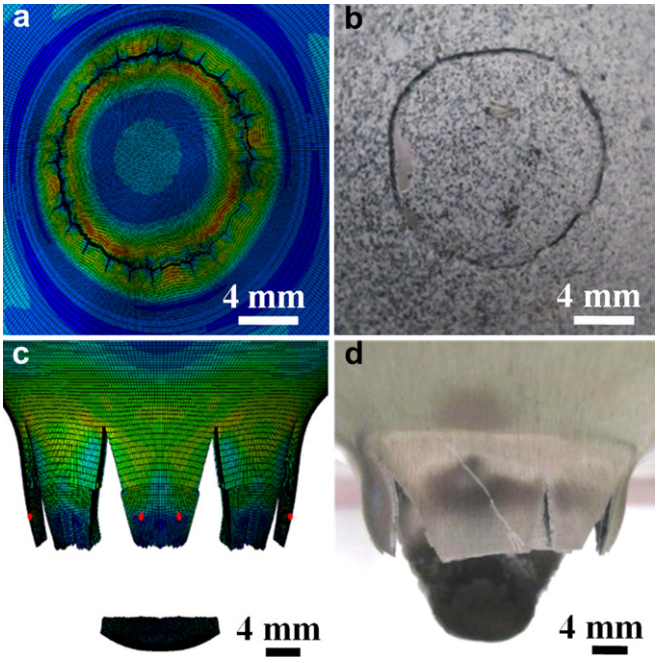

Fig. 15. Numerical and experimental failure shape of: (a, b) C^1_{2+1}; (c, d) C_{1+1} targets.

5.3. Residual deformation profiles and energy mapping

In experimental and numerical results, the maximum projectile displacement during the impact is higher than the maximum residual indentation (average of +20% for the experimental data and +10% for the numerical analysis). This phenomenon is due to the target elastic springback in the third impact stage (see Figs. 11 and 12). The results from Table 2 also show that the model underestimates the maximum projectile penetration during the impact (average gap of 10% for the B and C groups), while the maximum target indentation is very well reproduced (average gap of 2%).

Several deformation profiles are given in Fig. 16 for A and C family targets. Note that the numerical C^1_{2+1} and A_{2+2} profiles are very close to the experimental ones. Moreover, the maximum indentation of these two targets is similar (about 31 mm) in spite of their different thicknesses (3 and 4 mm respectively). This is due to the A_{2+2} sample momentum at the vicinity of the boundary condition, which is not observed in bigger targets because of inertial effects. A significant gap can be observed between the experimental and numerical profiles of the A_{2+1} target. This difference is probably due to the sliding of the sample near the plate-support contact which is higher in the reality than in the

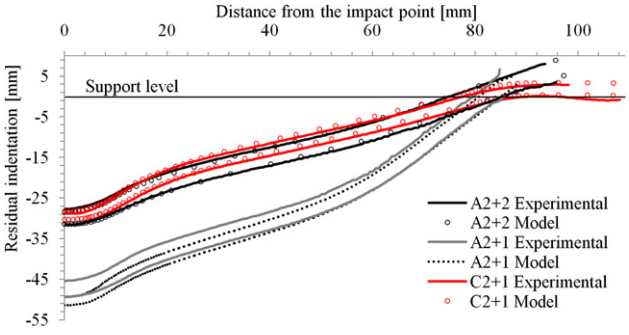

Fig. 16. Numerical and experimental deformation profiles after impact.

model. Thus, a decrease of the target thickness leads to a 30% indentation increase (comparison between A_{2+2} and A_{2+1}), as well as a decrease of the plate dimension (comparison between A_{2+1} and C^1_{2+1}).

In the numerical model, the initial projectile kinetic energy is transferred to the target mainly through elastic and plastic energies. Additional energies like mesh stabilization energy, viscous or frictional energy are negligible. In the case of C^1_{2+1} target, the experimental absorbed energy reaches 954 J at the end of impact (see Table 3). The energy absorbed by the structure in the associated numerical model reaches 848 J (90% of the initial kinetic energy of the projectile) in the last impact step (projectile rebound). This remaining energy corresponds to elastic energy, either retransmitted to the projectile into kinetic energy, or blocked in the sample. The 2-mm thick front plate and the 1-mm thick rear plates absorb 570 J and 275 J respectively through plasticity (95% and 93% of the total absorbed energy of the plate). Thus, the absorbed energy quantity is very close for the two plates, considering their respective thicknesses. The energy per unit volume distribution is given in Figs. 17b and 18 for different target zones

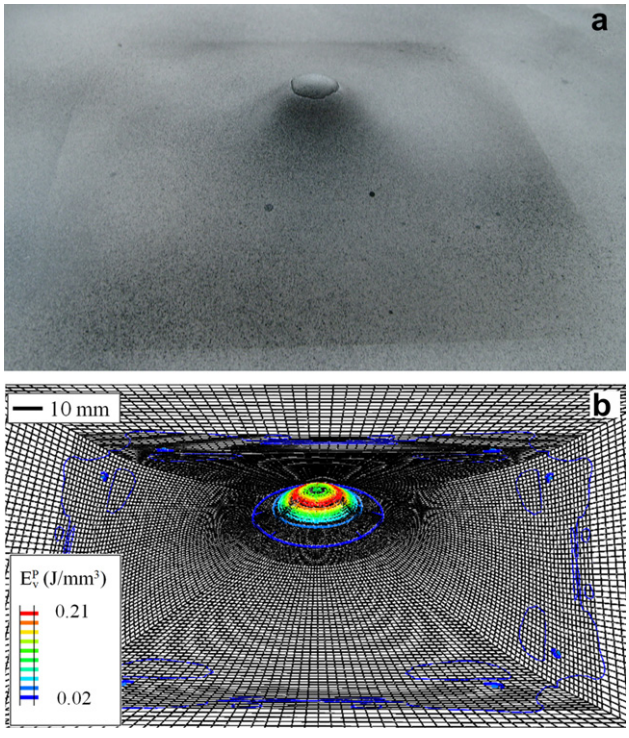

Fig. 17. (a) C^1_{2+1} target shape; (b) C^1_{2+1} numerical plastic energy per unit volume.

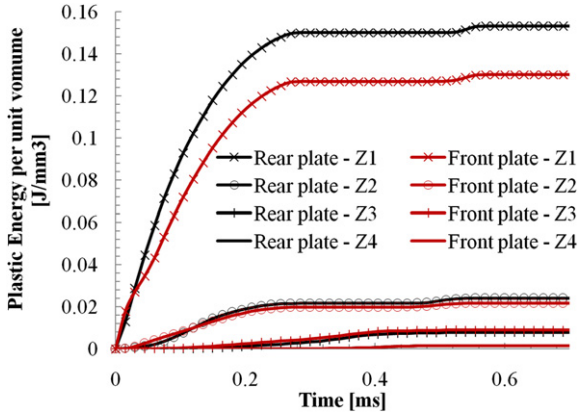

Fig. 18. Plastic energy repartition for each layer in different target zones (C^1_{2+1}).

Z1−Z4 (see Fig. 5). The rear of the back plate under the projectile is characterized by a large amount of energy absorption (see Figs. 8, 17a and b). The maximum value of plastic energy absorbed per unit volume reaches 0.225 J/mm^3 in the localized necking zone, with an average value of 0.15 J/mm^3 in the totality of the Z1 zone (see Fig. 18). The plastic energy absorbed per unit volume decreases rapidly with the distance from impact. Considering the association of the two layers, respectively 15%, 20%, 52% and 13% of plastic energy is absorbed in the Z1−Z4 zones, corresponding to 0.7%, 6%, 38.2% and 55.6% respectively of the total volume of the target.

6. Structure optimization

A further investigation has been conducted to optimize aluminum samples submitted to impact. Two options have been identified:

- Material optimization: optimal choice of the key material parameters.
- Geometry optimization: layered and monolithic plate results, total thickness influence.

6.1. Material optimization

The first way of investigation deals with the target material properties, defined through the flow stress and the fracture strain. The problem is to choose the appropriate materials to improve the armor resistance. On the one hand, the flow stress effect is highlighted in both the residual profile and the contact forces. High yield stresses reduce the global out-of-plane indentation of the target and increase the contact force. On the other hand, the fracture strain determines the onset of rupture and it is obvious that ductile materials are more likely to delay the perforation and to resist against the impact. However, these two parameters are commonly linked within the available material. High yield stress material generally has low fracture strain and shows early brittle fracture, whereas ductile material has low yield stress which induces high indentation. Such observation implies to search for a balance between stress yield and fracture strain for selecting the suitable material.

Note that the evolution of the fracture strain with the strain rate appears to be a key material parameter. This assumption has been verified with an additional impact simulation on a virtual B_{2+2} target composed of 2-mm thick superposed AA5086 plates without bonding. This structure total thickness is above the critical thickness of 3 mm and is expected to resist against the impact under the

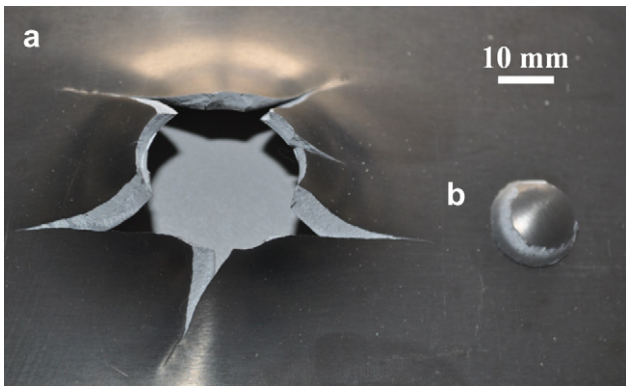

Fig. 19. (a) Rupture shape of a 3-mm thick AA2017 target; (b) circular cap formation.

same experimental conditions (no rupture of A_{2+2} and C_3 samples). The simulation has been performed with an initial kinetic energy similar to the A_{2+2} case, but with a projectile of 1 kg launched at 45 m/s (case 1). Another model with the same configuration has been implemented using the usual impact parameters (projectile of 127 g launched at 127 m/s: case 2). In the first case, the low projectile initial velocity leads to a global strain rate decrease which causes the total rupture of the two skins after only 400 μs. At this point, the remaining projectile velocity is 40 m/s (only 20% of the initial kinetic energy is absorbed). In the second case, the rupture criterion reaches 0.93 (rear of the first plate) at the end of the impact (1.3 ms) and the velocity rebound is 20 m/s. At the onset of rupture (case 1), the typical strain rate values reach 800 s^{-1} at the rear of the front plate (critical zone). In the case 2, the strain rate is about 1500 s^{-1} in the same zone after an impact duration of 400 μs.

An additional impact test has been conducted on a monolithic 3-mm thick 2017 aluminum target with a 300-mm edge. This alloy is characterized by high tensile properties with a yield stress comprised between 230 and 260 MPa and an ultimate stress around 390 MPa (depending on heat treatment). Moreover, there is no particular strain rate effect reported in the literature concerning this alloy. The experimental conditions are the same as those described in Section 2.1 and the initial velocity reaches 117.7 m/s (i.e. 880 J impact energy). The target is perforated after impact (see Fig. 19a) and shows local damages: initial circular crack at the rear of the back face, petals and circular cap formation with a 16-mm diameter (Fig. 19b).

Note that the C_3 case (same thickness and AA5086 alloy with a 400-mm edge) which is close to this configuration, showed no rupture and no crack initiation after an impact velocity of 118 m/s. This result underlines the importance of the material properties in terms of armor optimization. The main criteria are therefore to choose materials with the right ductility/strength proportion under quasi-static tensile tests (depending obviously on the chosen impact conditions) and with positive strain rate sensitivity.

6.2. Geometry optimization

Numerical simulations have been performed on different target stratifications ($2 + 1$, $1 + 2$ and 3×1) and compared to a 3-mm thick monolithic structure (C_3 or B_3) in order to study the effect of stratification. Two models have been implemented, one using the initial velocity of the corresponding experimental case as input (case 1) and the other using a constant initial velocity of 125 m/s for each configuration, to evaluate the stratification effect only (case 2).

In the first case, the model predicts the structure resistance, which is confirmed by the associated experimental tests. The mapping of F obtained by modeling shows that the structure works in bending for thick or monolithic plates (value of the criterion increasing with thickness, as shown in Fig. 20a) and tends to work as a membrane with the stratification (low variation of criterion value in each layer in Fig. 20b). The rupture criterion value tends to decrease with stratification (from −1% to −8% with a 2-layer stratification and −16% with a 3-layer stratification). The maximum criterion values obtained are 0.97, 0.96, 0.9 and 0.82 respectively for C_3, B_{2+1}, B_{1+2} and $B_{3\times1}$. However, these results also depend on the initial impact velocity associated with each experiment.

To evaluate properly the stratification effect, the same structures have been numerically impacted with the same initial projectile velocity. An additional monolithic structure with a 3-mm total thickness B_3, has been modeled and compared with layered targets. The same tendency as described in case 1 is noticed (global decrease of F with the stratification), but in lower proportions as observed previously: from +2 to −5% with a 2-layer stratification and −8% with a 3-layer stratification (respective criterion values of 0.89, 0.92, 0.97 and 0.99 for $B_{3\times1}$, B_{1+2}, B_3 and B_{2+1}). When the maximum criterion value of 0.89 is reached in the $B_{3\times1}$ configuration, the plastic energy absorbed in the target is 295 J (30% of the initial kinetic energy). For the same criterion value in the other configurations, the plastic energies absorbed are evaluated to 225, 260 and 310 J for B_{2+1}, B_{1+2} and B_3 (23%, 26 and 31% respectively of the initial projectile energy). Note the particular case of the B_{2+1} configuration which appears to give results quite similar to those of the monolithic structure. In comparison, the B_{1+2} target shows better results than the B_{2+1} configuration with respective criterion values of 0.92 and 0.99. The contact force versus displacement is plotted in Fig. 21. Note that the global behavior of targets with a same total thickness is very similar, with the exception of the initial peak force which tends to decrease with the increasing number of stratifications. The contact force begins to decrease when the projectile displacement reaches 28 mm, which corresponds to the global structure reaction. It can be seen on Fig. 21 that this decrease depends on the number of stratifications (46% for a monolithic structure, average of 66% with a 2-layer stratification and 84% with a 3-layer stratification).

To complete this analysis, an additional layered configuration has been also tested with a lower total thickness of 2.5 mm

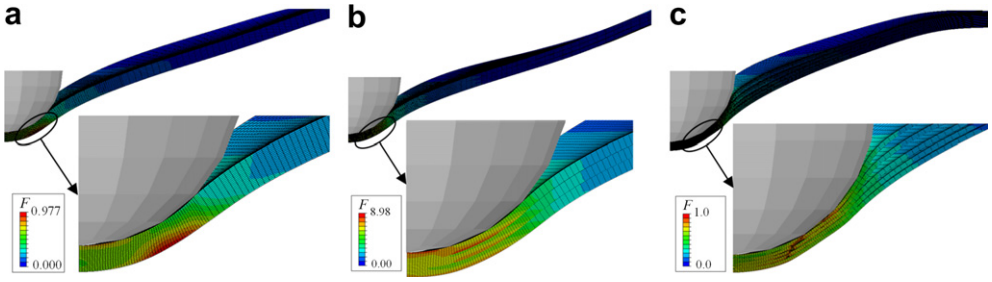

Fig. 20. Rupture criterion mapping for different targets: (a) C_3; (b) $B_{3\times1}$ (case 1); (c) $B_{5\times0.5}$.

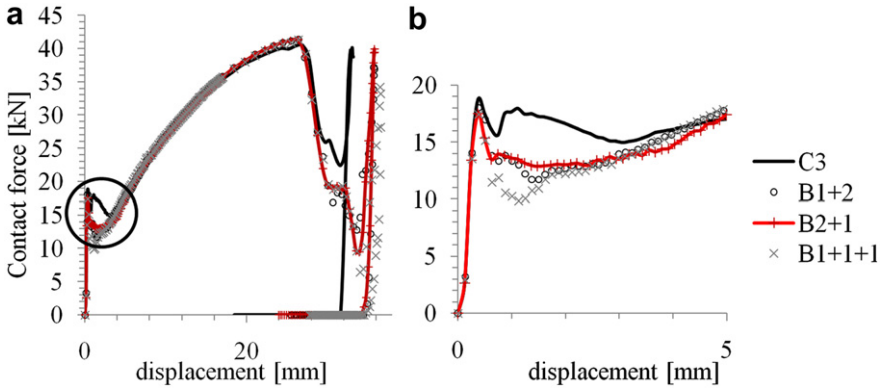

Fig. 21. (a) Numerical force vs. displacement curves (case 2); (b) zoom at the onset of impact.

composed of five 0.5-mm thick layers. The simulation predicts the rupture of the first 4 layers after 250 μs, with a remaining projectile velocity of 80.7 m/s. The numerical calculations then become instable because deleted elements cause problems in the contact algorithm. The experimental rupture shape can be seen in Fig. 3b and the numerical profile is given in Fig. 20c. These results confirm the thickness limit of 3 mm to avoid the structure perforation. At the same time, this case corresponds also to a balance limit to be found between low and high flow stresses, associated respectively with high rupture strains and plate stiffness (see discussion in the previous section). This case shows that even with a lower flow stress of the 0.5-mm thick plates (compared to the 1- and 2-mm thick plates as shown in Fig. 8) and the target stratifications, these effects are not enough to balance the thickness decrease and to avoid structure perforation. The decrease of the layer thickness can also lead to a greater dependency of the material local defects which may accelerate the rupture initiation.

7. Conclusions

Experimental impact tests have been conducted on aluminum targets with different dimensions, thicknesses and stratifications. A numerical analysis using the finite element code ABAQUS/Explicit model has been implemented using the Johnson–Cook flow stress and rupture models. The results obtained from the numerical analysis were consistent with the experimental results in terms of rupture prediction, projectile velocity evolution, and residual deformation profiles. The comparison and analysis of results lead to the following conclusions:

1. The total target thickness strongly influences the impact performances, with a critical value set to 3 mm. Below this limit, structures failed through plug and petals formation, which is typical of ductile materials.
2. A minimum sample dimension with a 300-mm edge has been identified to avoid excessive rotations of the plates in the vicinity of the boundary conditions, which are not representative of real aeronautical structures.
3. The presence of adhesive bond between the layers or a simple superposition appears to give close experimental results. However, in the numerical model, the critical zone location moves from the rear of the last layer (with bonding) to the rear of the thicker layer (without bonding) or is at the rear of the first layer in case of identical layers.
4. The plate stratification appears to be a second order effect according to the experiments and the numerical modeling. A slight improvement is observed in the model when layering the targets. The layer behavior is modified from bending to membrane reaction. This results in a slight decrease of the rupture criterion value (−5% and −8% for B_{1+2} and $B_{3\times1}$ compared to B_3) and a slight increase of the target indentation (+2% and +4%).
5. Regarding the material selection, ductile materials show best impact results due to their ability to spread the plastic deformations which lead to a larger amount of absorbed energy. Moreover, the numerical analysis showed a clear influence of the strain rate evolution. Alloys with positive strain rate sensitivity have good impact performances due to the rupture initiation delay.

Acknowledgement

The authors want to thank the National Research Agency for the financial support through the MANSART Project based on saNdwichSARchitecTuredMAterials. This work was granted access to the HPC resources of CALMIP under the allocation 2012-P1026.

References

[1] Clausen AH, Børvik T, Hopperstad OS, Benallal A. Flow and fracture characteristics of aluminium alloy AA5083-H116 as function of strain rate, temperature and triaxiality. Materials Science and Engineering A – Structural Materials 2004;A364:260–72.
[2] Børvik T, Hopperstad OS, Pedersen KO. Quasi-brittle fracture during structural impact of AA7075-T651 aluminium plates. International Journal of Impact Engineering 2010;37:537–51.
[3] Børvik T, Clausen AH, Hopperstad OS, Langseth M. Perforation of AA5083-H116 aluminium plates with conical-nose steel projectiles – experimental study. International Journal of Impact Engineering 2004;30:367–84.
[4] Børvik T, Langseth M, Hopperstad OS, Malo KA. Perforation of 12 mm thick steel plates by 20 mm diameter projectiles with flat, hemispherical and conical noses. Part I: experimental study. International Journal of Impact Engineering 2002;27:19–35.
[5] Gupta NK, Iqbal MA, Sekhon GS. Effect of projectile nose shape, impact velocity and target thickness on deformation behavior of aluminum plates. International Journal of Solids and Structures 2007;44:3411–39.
[6] Børvik T, Hopperstad OS, Berstad T, Langseth M. Perforation of 12 mm thick steel plates by 20 mm diameter projectiles with flat, hemispherical and conical noses. part II: numerical simulations. International Journal of Impact Engineering 2002;27:37–64.
[7] Teng X, Wierzbicki T. Evaluation of six fracture models in high velocity perforation. Engineering Fracture Mechanics 2006;73:1653–78.
[8] Grytten F, Børvik T, Hopperstad OS, Langseth M. Low velocity perforation of AA5083-H116 aluminium plates. International Journal of Impact Engineering 2009;36:597–610.
[9] Grytten F, Børvik T, Hopperstad OS, Langseth M. Quasi-static perforation of thin aluminium plates. International Journal of Impact Engineering 2009;36:486–97.
[10] Iqbal MA, Chakrabarti A, Beniwal S, Gupta NK. 3D numerical simulations of sharp nosed projectile impact on ductile targets. International Journal of Impact Engineering 2010;37:185–95.
[11] Arias A, Rodríguez-Martínez JA, Rusinek A. Numerical simulations of impact behaviour of thin steel plates subjected to cylindrical, conical and

hemispherical non-deformable projectiles. Engineering Fracture Mechanics 2008;75:1635–56.
[12] Bao Y, Wierzbicki T. On the cut-off value of negative triaxiality for fracture. Engineering Fracture Mechanics 2005;72:1049–69.
[13] Iqbal MA, Gupta NK. Energy absorption characteristics of aluminum plates subjected to projectile impact. Latin American Journal of Solids and Structures 2008;5:259–87.
[14] Corbett GG, Reid SR, Johnson W. Impact loading of plates and shells by free-flying projectiles: a review. International Journal of Impact Engineering 1996;18:141–230.
[15] Corran RSJ, Shadbolt PJ, Ruiz C. Impact loading of plates: an experimental investigation. International Journal of Impact Engineering 1983; 1:3–22.
[16] Teng X, Dey S, Børvik T, Wierzbicki T. Protection performance of double-layered metal shields against projectile impact. Journal of Mechanics of Materials and Structures 2007;2:1307–28.
[17] Dey S, Børvik T, Teng X, Wierzbicki T, Hopperstad OS. On the ballistic resistance of double-layered steel plates: an experimental and numerical investigation. International Journal of Solids and Structures 2007; 44:6701–23.
[18] Teng X, Wierzbicki T, Huang M. Ballistic resistance of double-layered armour plates. International Journal of Impact Engineering 2008;35:870–84.
[19] Johnson GR, Cook WH. Fracture characteristics of three metals subjected to various strains, strain rates, temperatures and pressures. Engineering Fracture Mechanics 1985;21:31–48.
[20] Børvik T, Hopperstad OS, Berstad T, Langseth M. European Journal of Mechanics A/Solids 2001;20:685.
[21] Naka T, Yoshida F. Journal of Materials Processing Technology 1999;89/90:19.
[22] Wagenhofer M, Erickson-Natishan MA, Armstrong RW, Zerilli FJ. Scripta Materialia 1999;41:1177.
[23] Warren TL, Tabbara MR. Simulations of the penetration of 6061-T6511 aluminum targets by spherical-nosed VAR 4340 steel projectiles. International Journal of Solids and Structures 2000;37:4419–35.
[24] Camacho GT, Ortiz M. Adaptive Lagrangian modeling of ballistic penetration of metallic targets. Computer Methods in Applied Mechanics and Engineering 1997;142:269–301.